

Classification and Causes of East Asian Marine Heatwaves during Boreal Summer

HYOEUN OH,^a GO-UN KIM,^a YONG SUN KIM,^b JAE-HEUNG PARK,^c CHAN JOO JANG,^b YONGCHIM MIN,^a HYUNJUNG JUN,^a AND JIN-YONG JEONG^a

^a *Marine Disaster Research Center, Korea Institute of Ocean Science and Technology, Busan, South Korea*

^b *Ocean Circulation Research Center, Korea Institute of Ocean Science and Technology, Busan, South Korea*

^c *Division of Environmental Science and Engineering, Pohang University of Science and Technology (POSTECH), Pohang, South Korea*

(Manuscript received 15 May 2022, in final form 26 August 2022)

ABSTRACT: Marine heatwaves (MHWs) are among the most severe climatic events under global warming conditions; they damage marine ecosystems and result in socioeconomic losses. In East Asia, the sea surface temperature (SST) has increased significantly and is projected to increase further. Considering such increases in SST over East Asia, studies on MHWs are needed to minimize the damage caused. In this study, we classified the spatiotemporal characteristics of East Asian MHWs during boreal summer with a self-organizing map for 39 years (1982–2020) and determined their unexplored possible mechanisms. Four dominant modes of MHWs across East Asia were identified: the 1) Subtropical Gyre, 2) East China Sea, 3) East Sea/Japan Sea, and 4) Yellow Sea modes. The total annual number of MHW days has increased by about $1.23 \text{ days yr}^{-1}$. The significant trend is mainly determined by the Subtropical Gyre mode, whereas other modes do not exhibit significant trends. We found that the East China Sea mode could be attributed to a strong East Asian summer monsoon via ocean stratification by the low-salinity water from the Yangtze (Changjiang) River. The East Sea/Japan Sea and Yellow Sea modes could be linked to remote forcings over the subtropics, leading to persistent anticyclonic circulation over East Asia. The anomalous anticyclone contributed to the MHW occurrences by enhancing downward shortwave radiation and reducing entrainment cooling caused by Ekman downwelling. These findings have important implications for distinguishing the characteristics of East Asian MHWs and reveal the possibility of predicting them by identifying their precursors.

SIGNIFICANCE STATEMENT: This study aimed to better understand East Asian marine heatwaves (MHWs) and their causes. We utilized a self-organizing map to classify four patterns of MHWs during boreal summer across East Asia—the Subtropical Gyre, East China Sea, East Sea/Japan Sea, and Yellow Sea modes. We found that enhanced shortwave radiation and latent heat flux play an important role in modulating MHWs in East Asia. A reduced vertical-mixing-amplified ocean warming, and the ocean dynamics drove different temporal evolutions of the MHWs among the four modes. We also identified the potential precursors, which would help in improving the future prediction of MHWs in East Asia.

KEYWORDS: Atmosphere-ocean interaction; Extreme events; Heat budgets/fluxes; Sea/ocean surface

1. Introduction

A marine heatwave (MHW) occurs when ocean water temperatures are persistently hotter than average for days to months, which can severely impact marine ecosystems and result in socioeconomic losses. For example, severe MHWs trigger coral bleaching (Frölicher and Laufkötter 2018; Hughes et al. 2018), and excessively warm water temperatures can reduce biodiversity and the abundance of nutrient-competing phytoplankton species, resulting in the closure of fisheries (Gao et al. 2021). The MHWs differ from the atmospheric heatwaves in terms of location and duration of their occurrence because the ocean variability has longer time scales than the atmosphere due to ocean inertia (Hobday et al. 2016). The MHWs have become longer-lasting and more frequent over the past few decades and are projected to further

strengthen due to global warming (Frölicher et al. 2018; Qiu et al. 2021; Yao et al. 2020).

The boreal summer sea surface temperatures (SSTs) of the East Asian marginal seas (EAMS)—the Yellow Sea, East/Japan Sea, and East China Sea—have increased significantly over the past few decades (up to $0.58^\circ\text{C decade}^{-1}$) compared to the global mean ($0.15^\circ\text{C decade}^{-1}$) (Belkin 2009). Several studies have focused on the MHWs across East Asia (Li et al. 2019; Liu et al. 2022), since record-breaking SSTs have frequently occurred across East Asia in the twenty-first century (Yan et al. 2020). Gao et al. (2020) showed that extreme MHWs occurred in the East China Sea and the southern Yellow Sea in three recent summers (2016–18). These recent increases in MHWs across East Asia are attributed to mean warming and SST variability changes, unlike the global ocean, where MHWs are mainly affected by the increase in mean SST (Oliver 2019). Overall, the EAMS are among the most

^a Denotes content that is immediately available upon publication as open access.



This article is licensed under a Creative Commons Attribution 4.0 license (<http://creativecommons.org/licenses/by/4.0/>).

Corresponding author: Jin-Yong Jeong, jyjeong@kiost.ac.kr

vulnerable marine areas to climate change, especially with respect to the intensity of MHWs (Holbrook et al. 2019).

The potential factors influencing MHWs have been studied from atmospheric perspectives, and both the shortwave radiation from reduced cloud cover and the latent heat flux from weakened wind speeds have been shown to play essential roles in driving MHWs (Amaya et al. 2020; Bond et al. 2015; Li et al. 2022). Other studies have shown that MHWs are triggered by oceanic dynamics, such as current anomalies and reduced vertical mixing (Feng et al. 2013; Gao et al. 2020). Moon et al. (2019) displayed the contribution of freshwater flux to MHWs across the East China Sea in boreal summer. They revealed that the salinity-stratified mixed layer enhances SST warming by restricting heat exchanges and vertical mixing. Furthermore, Yao and Wang (2021) showed that both increased solar radiation and weakened upwelling contribute to basinwide severe summer MHWs in the South China Sea. Lee et al. (2020) classified the atmospheric and oceanic modes of the boreal summer MHWs across East Asia on the interannual time scale and investigated linkages with El Niño–Southern Oscillation (ENSO) phases and transitions; they showed that the transition phase from El Niño to La Niña plays an important role in maintaining the subtropical high. The sustained subtropical high suggests that shortwave radiation contributes to the generation of warm SST (Kuroda and Setou 2021; Yao and Wang 2021). As previous studies have focused on individual MHW events (Gao et al. 2020; Li et al. 2022; Oliver et al. 2017; Yan et al. 2020) or the seasonal to interannual characteristics and variability of MHWs (Lee et al. 2020; Yao and Wang 2021), the fundamental physical processes underlying these phenomena in EAMS remain poorly understood. Additionally, studies on the spatiotemporal distribution of East Asian MHWs are lacking.

As artificial neural networks, the self-organizing maps (SOMs) are governed by nonlinear processes; it is advantageous to effectively capture spatiotemporal patterns from nonlinear input data (Kohonen 1990). The application of SOMs has become popular in climate research, such as in studies on the East Asian summer monsoon (EASM; Chu et al. 2012; Oh and Ha 2015), typhoons (Kim and Seo 2016), and ENSO (Johnson 2013). Using the SOMs, Oliver et al. (2018) identified 12 MHWs over eastern Tasmania in Australia and showed their associated oceanic and atmospheric circulation patterns. Schlegel et al. (2017) employed an SOM analysis to determine the specific physical processes of MHWs over the continental shelf of the northwest Atlantic. To date, there have been no studies in which clustering methods have been used to identify MHWs in East Asia or their physical mechanisms have been focused upon. Thus, we used SOM analysis to explore the regional characteristics of MHWs across the EAMS on a subseasonal time scale. This study aimed to determine the spatiotemporal characteristics of MHWs during boreal summer and to elucidate the factors contributing to their occurrence using reanalysis and observation data. We ultimately classified MHWs in East Asia into four modes and examined their physical mechanisms and causes and identified their precursory subtropical forcings.

2. Data and methods

a. Reanalysis datasets and observation data at Korea Ocean Research Stations

Daily SSTs were extracted from the National Oceanic and Atmospheric Administration (NOAA) Optimum Interpolation SST (OISST v2) dataset with a 0.25° resolution from 1982 to 2020 (Huang et al. 2021; Reynolds et al. 2007). Daily atmospheric reanalysis data on a $0.25^\circ \times 0.25^\circ$ grid, including geopotential height at 500 hPa, 10-m/850-hPa winds, surface net downward shortwave radiation, net upward longwave radiation, sensible heat flux, latent heat flux, and precipitation, were calculated from the hourly data of the European Centre for Medium-Range Weather Forecasts (ECMWF) Reanalysis v5 (ERA5) (Hersbach et al. 2020). This study used daily ocean data (temperature, salinity, and zonal and meridional velocities) obtained from the GLORYS12 reanalysis of the Copernicus Marine Environment Monitoring Service (CMEMS) on a $1/12^\circ$ horizontal grid, which covers the period from 1993 to 2020 (Jean-Michel et al. 2021). In this study, boreal summer [July–September (JAS)] MHWs during 1982–2020 were analyzed.

Three platforms from the Korea Ocean Research Stations (KORS)—Ieodo (32.12°N , 125.18°E ; established in June 2003), Gageocho (33.94°N , 124.59°E ; established in October 2009), and Socheongcho (37.42°N , 124.74°E ; established in October 2014)—which are used to monitor atmospheric and oceanic variability across multiple time scales (Ha et al. 2019; Y. S. Kim et al. 2019). These KORS platforms have been utilized to monitor extreme events in the ocean and atmospheric systems, such as steam fog (Heo et al. 2010; Yun and Ha 2022), tropical cyclones (Kwon et al. 2012; Moon and Kwon 2012), the EASM (Oh et al. 2014), air pollutants (Oh et al. 2020), and spring temperature evolution (Kim et al. 2022). As they provide data for understanding the characteristics of MHWs over the EAMS, this study utilized water temperature and salinity from Ieodo (measured at 4, 6, 9, 14, 18, 28, and 34 m) and Socheongcho stations (measured at 5, 7, 10, 15, 20, 30, and 40 m) during 25 June to 9 August 2016. The temporal interval for atmospheric and oceanographic variables was 1 and 10 min, respectively. Thus, we obtained daily atmospheric and oceanic variables by taking an average from 1 and 10 min.

b. Definition of MHWs and empirical orthogonal function-based SOM analysis

The MHWs can be detected when SSTs exceed the extreme ocean warming threshold and persist above this threshold for more than five days (Hobday et al. 2016). The threshold is defined as the seasonally varying 90th percentile by applying an 11-day window centered on each year's time for the baseline climatology of the daily SSTs. An additional threshold was used by considering their sizes; when the MHWs with a minimum size of approximately $30\,625\text{ km}^2$ ($175\text{ km} \times 175\text{ km}$) occurred in the EAMS ($20^\circ\text{--}50^\circ\text{N}$, $110^\circ\text{--}142^\circ\text{E}$), a day was chosen as an extreme MHW event affected by synoptic-scale weather systems. Consequently, 854 days were identified during boreal summer (JAS) for the period 1982–2020.

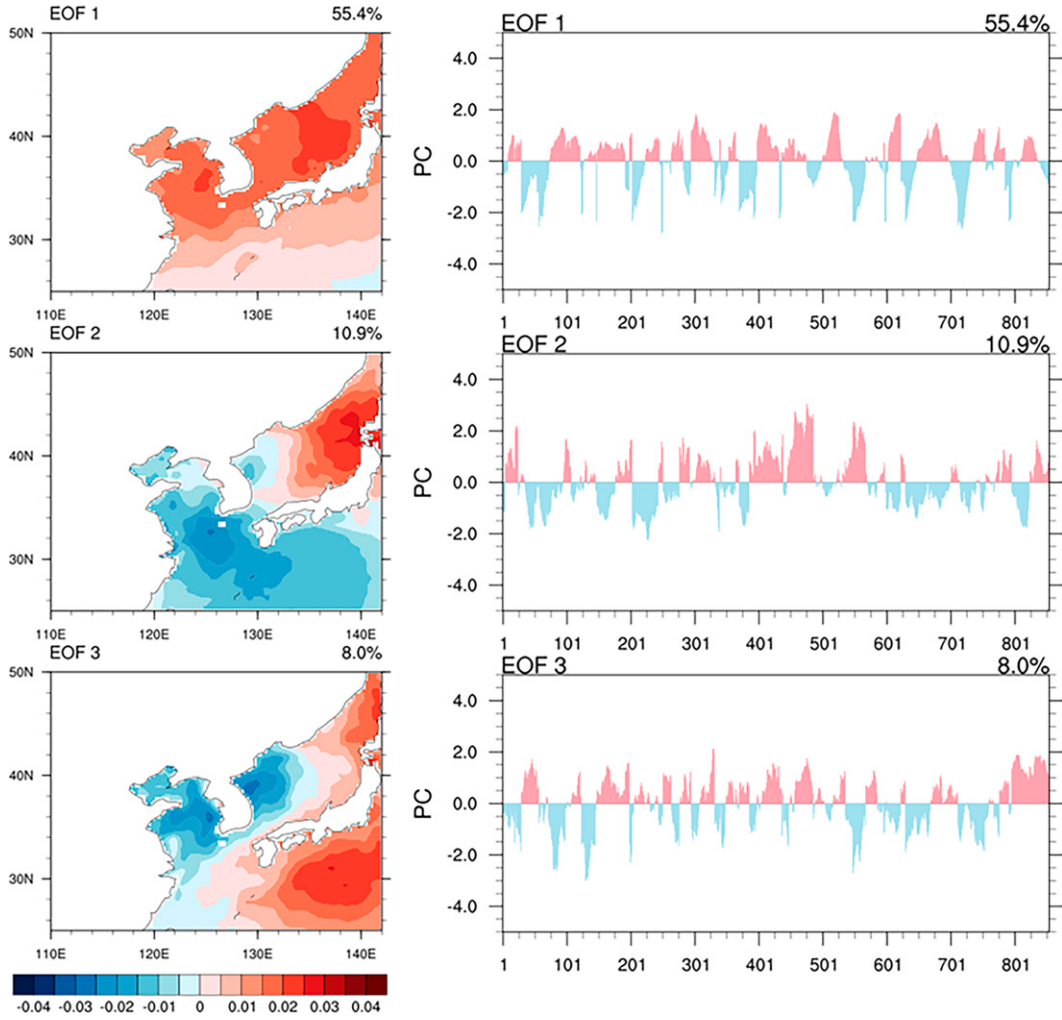


FIG. 1. Spatial patterns of the three dominant modes of anomalous sea surface temperatures (SSTs) for 854 marine heatwave (MHW) days in the empirical orthogonal function (EOF).

Before performing SOM analysis, we conducted an empirical orthogonal function (EOF) analysis with the anomalous SST pattern to obtain the dominant principal component (PC) time series of SSTs when MHWs occurred throughout the EAMS (Fig. 1). The three leading EOF modes had distinctive spatial patterns, and the associated PCs indicated how the amplitude of each EOF varied over time. The PCs contained information on the days on which SSTs were warm or cold, as well as their respective amplitudes. The first EOF mode (55.4%) represents a basin-scale pattern with concentrated loading over the eastern Yellow Sea and the eastern part of the East/Japan Sea, while the second (10.9%) is related to the east–west zonal dipole distribution of SSTs. The third mode (8.0%) shows relatively cool SST around the Korean Peninsula and warm SST across the western North Pacific (WNP). These three PCs were used as input vectors, combined with the north–south and east–west features of SST for SOM analysis.

To explore the spatiotemporal characteristics of MHWs across East Asia, we took advantage of SOM, which is an

unsupervised artificial neural network (Kohonen 1990) and is useful for visualizing a low-dimensional representation from large multidimensional input data. The SOMs were used to cluster the 854 MHWs into four modes based on their areas of occurrence to determine their subseasonal characteristics and relevant atmospheric and oceanic patterns. The SOMs are composed of input and competitive layers. In this study, **input vectors are the first three PCs!** The all the input vectors in the input layer were fully connected to the reference vectors in the competitive layer. The reference vectors were determined by weighting the coefficients using an iterative training process, which minimizes the Euclidean distance between the input and reference vectors. After training, the reference vectors were updated on the winning nodes (or best matching units), and the input vectors approached the positions that best represented them based on the least Euclidean distance (mapping process). **Four modes were defined by the user (Fig. 2).** A detailed discussion of the SOM analysis was presented by Chu et al. (2012). The modes consist of PC1,

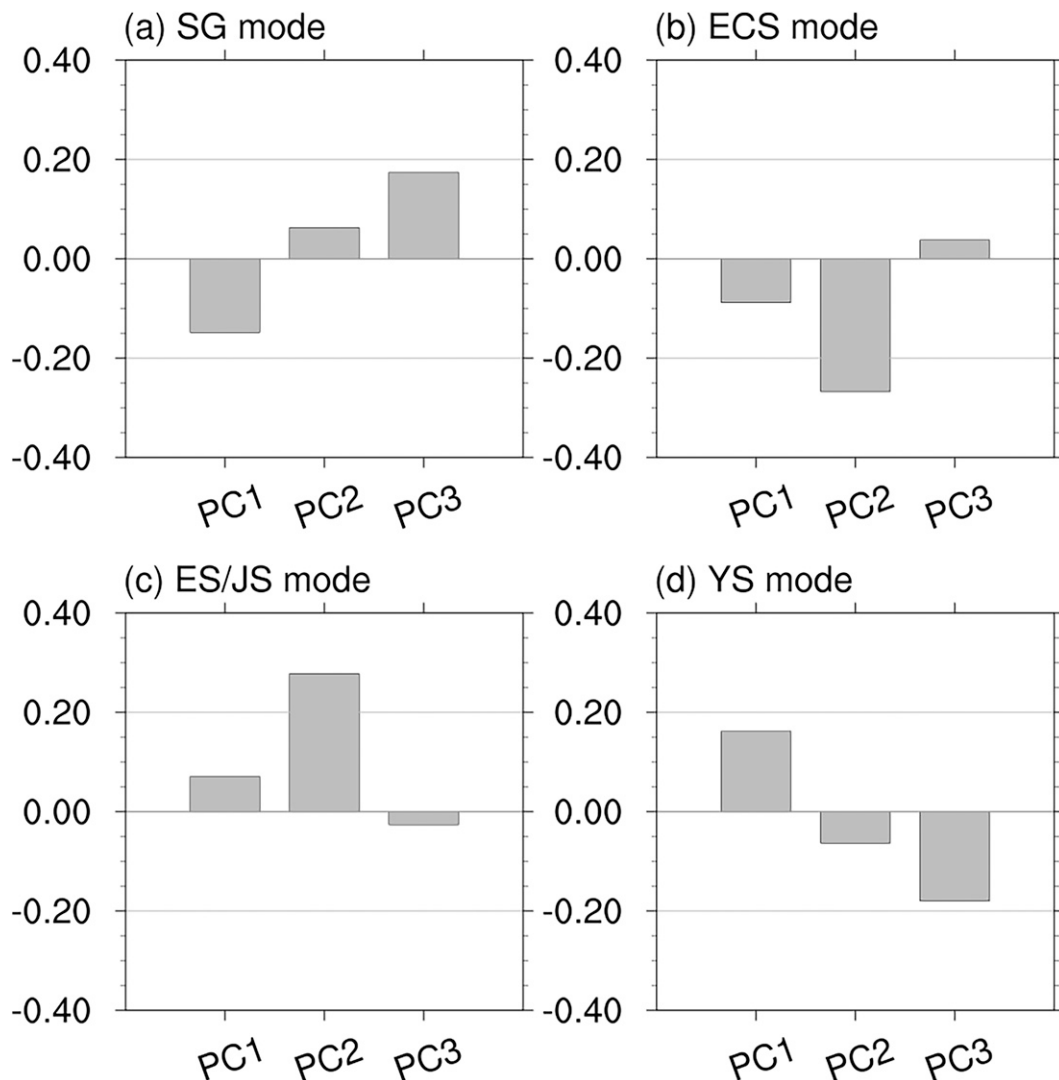


FIG. 2. Reference vectors (PC1, PC2, and PC3) recovered by self-organizing map (SOM) analysis for the (a) Subtropical Gyre (SG), (b) East China Sea (ECS), (c) East Sea/Japan Sea (ES/JS), and (d) Yellow Sea (YS) modes.

PC2, and PC3 (i.e., reference vector) representing themselves and are referred to as the Subtropical Gyre (SG), East China Sea (ECS), East Sea/Japan Sea (ES/JS), and Yellow Sea (YS) modes (Fig. 2). These are named after the characteristics or areas in which MHWs mainly occurred based on the spatial distribution of SSTs (Fig. 4).

A 2×2 map was created using the first three PCs of the SST for the 854 MHW days with the reference vectors. For example, PC1, PC2, and PC3 on 29 July 1983 were -0.66 , -0.86 , and -0.39 , respectively, which led this date to be classified as the second mode (the ECS mode) based on the least Euclidean distance (Fig. 2b). When the negative PCs were combined, the SST warming loading in the East China Sea could be estimated (Fig. 1). Thus, this map contains information about the clustered dates, and the composite of the classified dates provide the spatial structure for each mode.

3. Results

a. Characteristics and extraction of MHWs

The climatological summer SST across the EAMS showed a large meridional gradient ranging from 10° to 28°C for 30 years (Fig. 3a). The spatial distribution of the 90th percentile SST threshold was analogous to that of the climatological mean SST, but was approximately $0.9^\circ\text{--}2.0^\circ\text{C}$ higher than that shown by climatology (Fig. 3b). Moreover, the SST across East Asia was found to be significantly increasing with a rate up to $0.5^\circ\text{C decade}^{-1}$ since 1982 (Fig. 3c).

The characteristics of boreal summer MHWs across East Asia, including their frequency, duration, and maximum intensity for 1982–2020, are also shown in Fig. 3. The mean frequency is the average number of events, and the mean duration is the average length of the events. The maximum intensity is defined as the highest SST for each grid point during

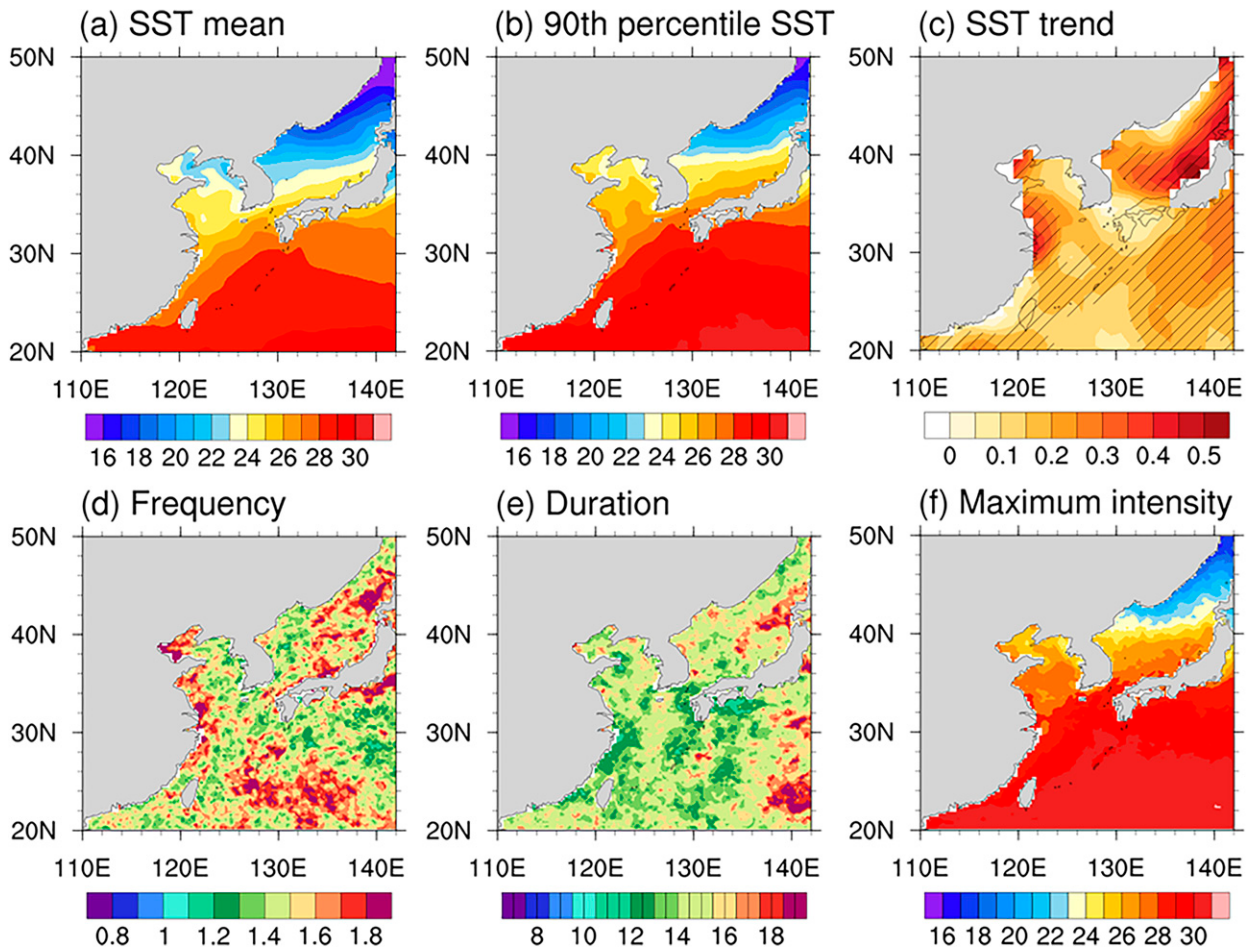


FIG. 3. Boreal summer [July–September (JAS)] (a) sea surface temperature (SST) ($^{\circ}$ C), (b) 90th percentile of daily SST ($^{\circ}$ C), (c) decadal trends in SST ($^{\circ}$ C decade $^{-1}$), (d) mean frequency of marine heatwaves (MHWs) (number of events), (e) mean duration of MHWs, and (f) maximum intensity of MHWs ($^{\circ}$ C) for 39 years from 1982 to 2020. The hatched lines in (c) indicate the significant area at the $p < 0.05$ level.

MHW. The MHW occurred 1.8 times on average each summer near the coasts of China and Japan (Fig. 3d). We also observed frequent MHWs along the Kuroshio Current, the WNP, and parts of the East/Japan Sea. The high-frequency MHWs along the coast of China could be attributed to short-lasting MHWs (Figs. 3d,e). The WNP and East/Japan Sea showed more frequent (>1.8 cases) and long-lasting MHWs (>18 days) (Figs. 3d,e). A trend of increasing mean MHW frequency and duration was apparent along the coast of China

and Japan (figure not shown), indicating that the MHWs have occurred more frequently and lasted longer in the past decades (Lee et al. 2020). The maximum intensity of MHWs was approximately 2–4.5°C higher than the climatological SST (Figs. 3a,f). The noticeable increases in the intensity tended to be affected by increasing mean SST north of 30°N (Figs. 3c,f). Overall, the EAMS are expected to be damaged by MHWs, along with the increase in mean SST in the future (Plecha and Soares 2020).

TABLE 1. Summary of mean days per event, the number of events, and total number of clustered days for the four modes derived via self-organizing map (SOM) analysis.

	Marine heatwave modes			
	SG (21.2%)	ECS (28.2%)	ES/JS (25.2%)	YS (25.4%)
Mean days per event	5.17	8.93	6.52	8.68
No. of events	35	27	33	25
Total No. of clustered days	181	241	215	217

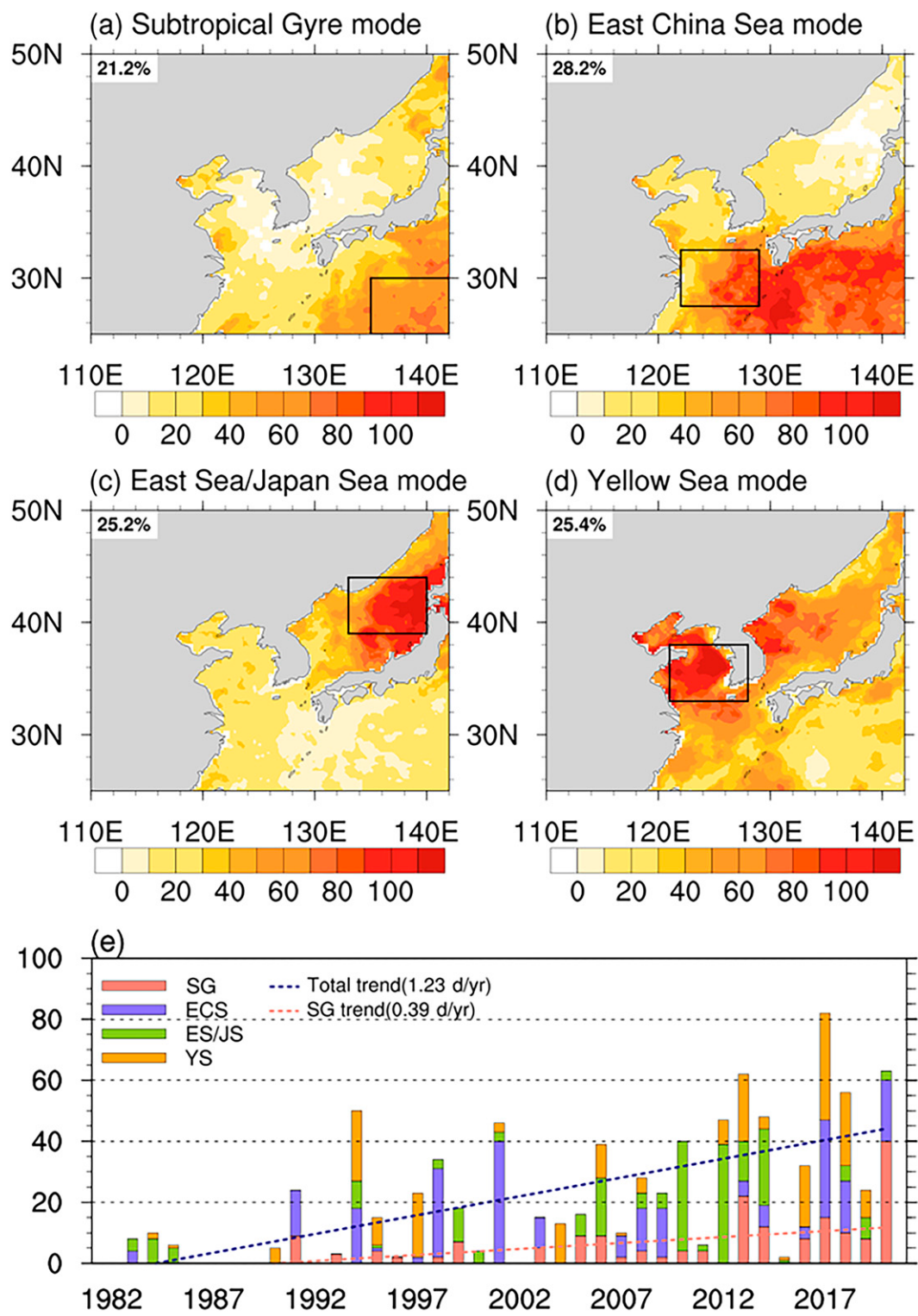


FIG. 4. Composite map of the number of marine heatwaves (MHWs; in days) in the (a) Subtropical Gyre (SG), (b) East China Sea (ECS), (c) East Sea/Japan Sea (ES/JS), and (d) Yellow Sea (YS) modes clustered by self-organizing map analysis. The areas over which MHWs occurred the most frequently for each mode were marked with black boxes: SG mode (25° – 30° N, 135° – 142° E), ECS mode (28° – 33° N, 122° – 129° E), ES/JS mode (39° – 44° N, 133° – 140° E), and YS mode (33° – 38° N, 121° – 128° E). (e) Interannual variability in the occurrences (days) of each mode, and trends for their overall MHWs (navy dashed line) and SG mode (pink dashed line).

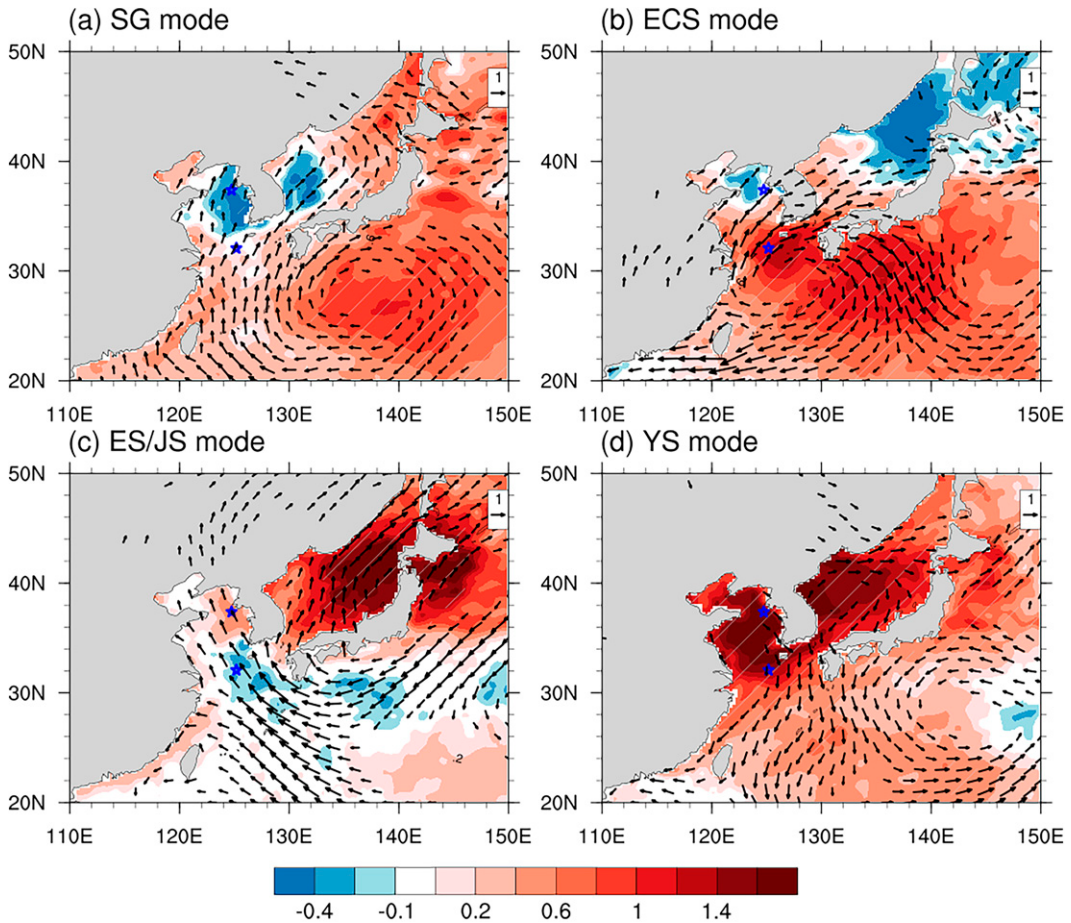


FIG. 5. Composite map of anomalous SST ($^{\circ}$ C) and 10-m wind ($m s^{-1}$) for the (a) Subtropical Gyre (SG), (b) East China Sea (ECS), (c) East Sea/Japan Sea (ES/JS), and (d) Yellow Sea (YS) modes. For wind vectors, only anomalous wind speeds $> 0.5 m s^{-1}$ are shown. The blue stars in (a)–(d) represent the Korean Ocean Research Stations (KORS) (Socheongcho and Ieodo, from top to bottom). The gray hatched lines indicate the significant area at $p < 0.05$.

Based on the definition of an MHW and our thresholds (see section 2b), the SOM analysis classified the 854 days recorded between 1982 and 2020 into four MHW modes: the SG (181 days), ECS (241 days), ES/JS (215 days), and YS (217 days) modes (Table 1). Here, the number of events was counted when MHWs were consecutively clustered into a particular mode without any break. The mean days per event were determined by dividing the total number of clustered days by the number of events. As a result, the SG mode showed the largest number of events and lasted for a shorter duration than other modes. The ECS mode occurred 27 times with a duration of approximately 8.93 days and is the longest-lasting MHW mode in East Asia. The ES/JS (YS) mode occurred 33 (25) times and lasted approximately 6.52 (8.68) days on average (Table 1).

Figure 4 displays the composite maps of the number of MHW days corresponding to the clustered dates of each mode. Among the 854 days, 21.2% were projected into the SG mode. The MHWs of the SG mode mainly occurred over the center of the WNP subtropical high (WNPSH) (Figs. 4a

and 5a). Thus, we can infer that the shortwave radiation and wind-induced Ekman downwelling could contribute to MHWs in this mode. The ECS mode accounted for 28.2% of the MHWs across East Asia, showing frequent MHWs in the East China Sea, and tended to cover areas such as the WNP; however, in this study, we focused on the MHWs in the East China Sea. In the ES/JS mode (25.2%), MHWs were mostly in the East/Japan Sea. The YS mode was observed in frequent MHWs in the Yellow Sea (25.4%). Based on our threshold, most MHWs occurred after the mid-1990s due to increases in mean SSTs across the EAMS (Fig. 4e). Prior to early 2000s, no MHWs occurred for 6 years. Since then, the total annual number of MHW days has increased by $1.23 \text{ days yr}^{-1}$. The most notable increase was observed in the SG mode ($0.39 \text{ days yr}^{-1}; p < 0.01$), while the other modes exhibited insignificant trends. The SG mode was analogous to a spatial distribution of SST trend (Fig. 3c), and the annual number of MHW days increased significantly during the analysis period, indicating that this mode may be linked to global warming. Note that, the occurrence of MHWs was considerably different from

→ in which sense?

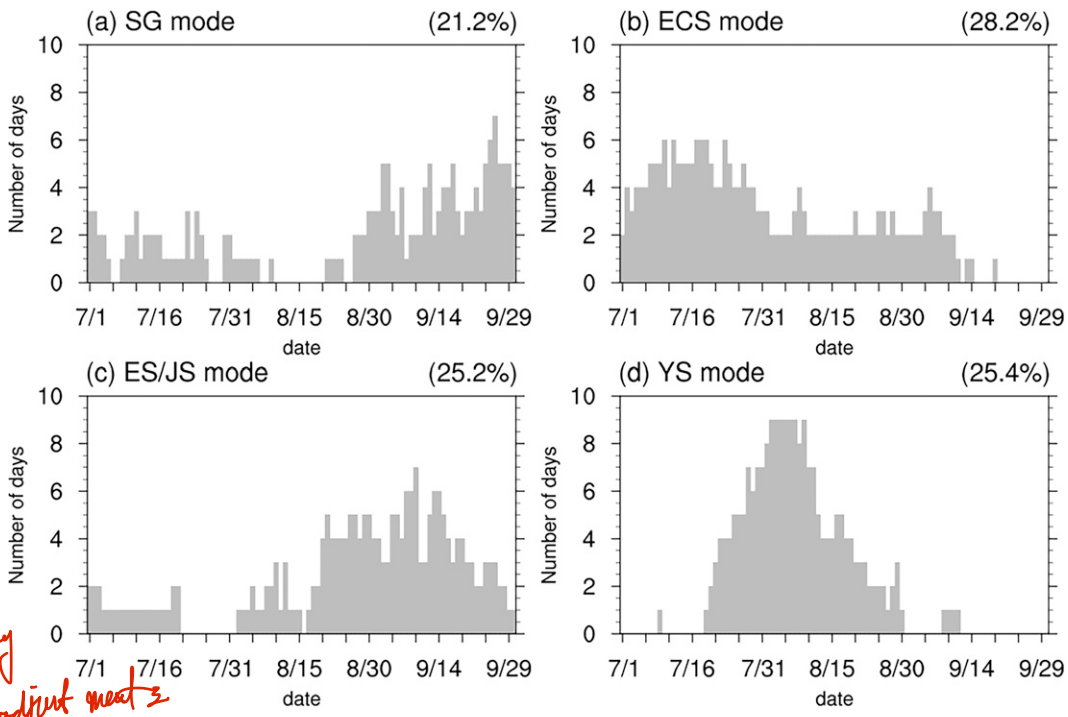


FIG. 6. Number of clustered days from 1 Jul to 30 Sep for the (a) Subtropical Gyre (SG), (b) East China Sea (ECS), (c) East Sea/Japan Sea (ES/JS), and (d) Yellow Sea (YS) modes.

atmospheric heatwave cases (Yeo et al. 2019). For example, the MHW occurred most frequently between 2017 and 2020, while a record-breaking atmospheric heatwave occurred in 2018 across East Asia (Ren et al. 2020).

The SST and low-level wind patterns associated with the four modes are shown in Fig. 5. An enhanced WNPSH coincided with regions of frequent MHWs and warm SST in the SG mode. This warm SST (1.16°C) was weaker than MHW-related warming in other modes. Having relatively cooler SST along the western coastal area of the Korean Peninsula, we rarely observed MHWs in the corresponding region (Figs. 4a and 5a). This SG mode occurred mainly in September, and approximately 30% of events occurred throughout July (Fig. 6a). The ECS mode, which was confined to July (Fig. 6a), showed a strong northwestward shift in WNPSH, resulting in a warm SST centered at the Ieodo station. The warming of this mode in East Asia is up to 1.41°C higher than average. In the ES/JS mode, hot conditions prevailing over the East/Japan Sea were associated with strong southwesterly winds from the subtropics (Fig. 5c); moreover, the period from late August to early September tended to cluster in this mode (Fig. 6c). The anomalous MHW-related SST was the warmest (up to 2.13°C) among the four modes. The YS mode frequently appeared from mid-July to late August (Fig. 6d). This mode exhibited an east–west zonal dipole pattern (i.e., anticyclonic circulation in the west and cyclonic circulation in the east), which was consistent with warm SST anomalies in the Yellow Sea and relatively cool SST anomalies in the WNP. The relevant SST increased up to 2.08°C when MHWs occurred in this mode.

The fixed ocean observing platforms of the KORS can help us better understand MHWs and verify whether the modes are classified well, especially for the ECS and YS modes, which resemble each other. We utilized data for the Ieodo (32.12°N , 125.18°E) and Socheongcho (37.42°N , 124.74°E) stations from 5 July to 9 August in 2016 to identify the classified MHW modes. In the case of the ECS mode, relative warming was observed in the south, with relative cooling in the north based on 35°N , compared to the YS mode (Figs. 5b,d and 7). For the YS mode, the MHWs contributed to SST warming throughout the Yellow Sea (Figs. 5d and 7). Data from the Ieodo station showed moderate to strong warming overall higher than the 90th percentile that persisted in ECS and YS modes from 21 July to 9 August (Fig. 7a). At the Socheongcho station, it was relatively cooler from 5 July to 3 August in the ECS mode and got warmer from 4 to 9 August in the YS mode (Fig. 7b). These features were also observed in the vertical structure of the water temperature and salinity (Figs. 7c,d). When MHWs occurred, a warm water temperature was maintained up to a depth of ~ 15 m at both the Ieodo and Socheongcho stations. Only the Ieodo station observed low-salinity water (< 30 psu) together with warm water to a depth of ~ 18 m. This suggests that the MHWs in the East China Sea could be characterized by low salinity because of freshwater input from rivers or precipitation itself (Figs. 7a,c). The low-salinity water could form a barrier, which plays an essential role in trapping heat in the surface layer, thereby reducing vertical mixing and impeding vertical heat exchanges, resulting in MHWs (Moon et al. 2019). The details of this part are provided in section 3b.

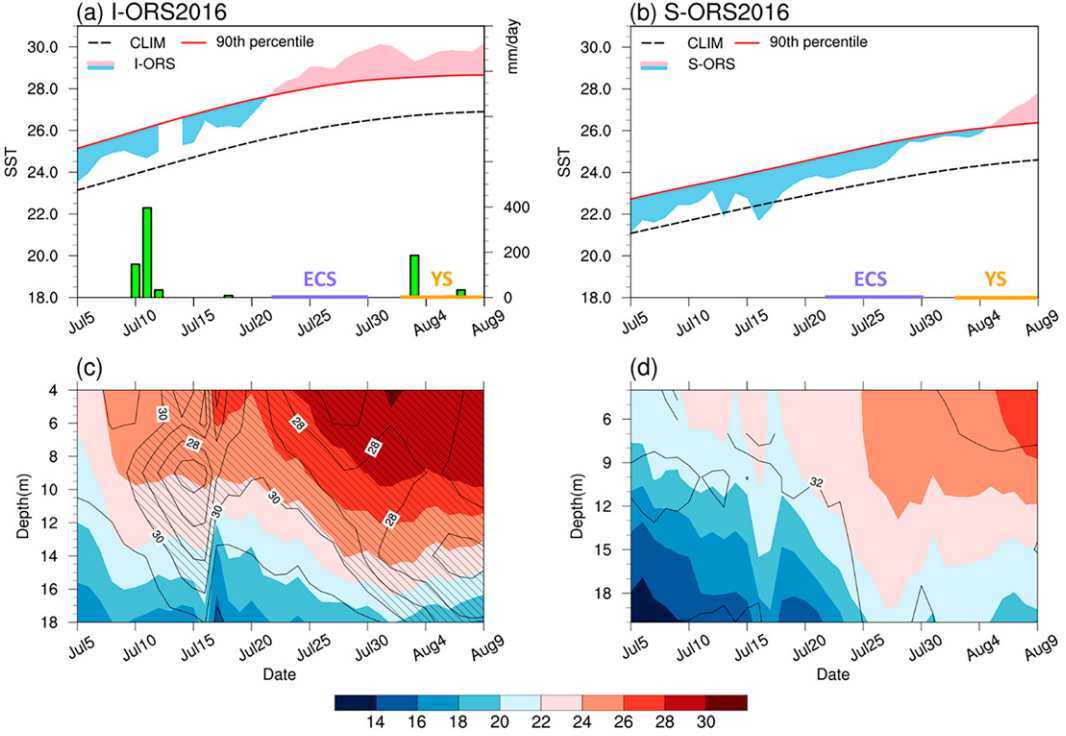


FIG. 7. Time series of sea surface temperature (SSTs) ($^{\circ}\text{C}$) and precipitation (mm day^{-1}) at the (a) Ieodo ocean research station (I-ORS) and (b) Socheongcho ocean research station (S-ORS) from 5 Jul to 9 Aug 2016 (pink and blue shadings). The precipitation was observed only at the I-ORS. The black dashed and red lines in (a) and (b) indicate the SST climatology and 90th-percentile threshold for the marine heatwaves during 1982–2011, respectively, which were obtained from OISST v2. Time-depth plots of mean water temperature ($^{\circ}\text{C}$; shading) and salinity (psu; contours) from the (c) I-ORS and (d) S-ORS data for the same period as in (a) and (b). The diagonal patterns indicate less than 30 psu, indicating low-salinity water. The period includes the ECS mode from 22 to 29 Jul and YS mode from 2 to 9 Aug, clustered by self-organizing map.

b. Physical mechanisms of MHWs in the four modes

To investigate the physical mechanisms of MHWs across East Asia, we explored the relative contribution of the air-sea heat exchange in the seas in which MHWs frequently occurred for each mode (Fig. 8). The areas over which MHWs occurred the most frequently for each mode were as follows: for the SG mode, 25° – 30°N , 135° – 142°E ; for the ECS mode, 27.5° – 32.5°N , 122° – 129°E ; for the ES/JS mode, 39° – 44°N , 133° – 140°E ; and for the YS mode, 33° – 38°N , 121° – 128°E (Fig. 4).

A mixed-layer heat budget analysis was performed to explore the relative contribution of different physical processes to MHWs (Moisan and Niiler 1998). Mixed-layer heat budgets can be expressed by the following equation:

$$\frac{\partial T_m}{\partial t} = -u_m \frac{\partial T_m}{\partial x} - v_m \frac{\partial T_m}{\partial y} - w_d \frac{(T_m - T_d)}{h_m} + \frac{Q_{\text{net}}}{\rho C_p h_m}, \quad (1)$$

where T_m , u_m , and v_m indicate the water temperature, zonal current, and meridional current averaged over the mixed-layer depth (17 m for SG mode, 13 m for ECS mode, 11 m for ES/JS mode, and 6 m for YS mode), respectively. We adapted the definition of the mixed-layer depth (h_m) from Liu et al. (2022), who defined it as the depth at which the water

temperature is 0.5°C lower than the surface value in each grid. The left-hand side of Eq. (1) shows the temperature tendency within the mixed layer, while the right-hand side shows the zonal, meridional advection, and vertical mixing of the mixed-layer water temperature; the final term represents the net surface heat flux. The vertical mixing term includes the effects of upwelling/downwelling as well as entrainment/detrainment. The terms w_d and T_d represent the vertical current velocity and water temperature, respectively, at a depth of 10 m below the bottom of the mixed layer, and Q_{net} denotes the sum of the net downward shortwave radiation, net upward longwave radiation, sensible heat flux, and latent heat flux at the surface. Positive values indicate a downward radiative heat flux. Also, ρ is the reference density of seawater (1025 kg m^{-3}) and C_p is the specific heat of seawater at a constant pressure ($3850 \text{ J kg}^{-1} \text{ }^{\circ}\text{C}^{-1}$). Due to the lack of daily subsurface ocean data, including water temperature and horizontal velocity for the entire analysis period, we used GLORYS12 data for the period 1993–2020. In addition, since no vertical velocity data are available, the oceanic physical processes, including the effects of vertical advection, mixing, and entrainment/detrainment, can be expressed as residuals. Here, we set the onset day of each MHW event as day 0 and analyzed the

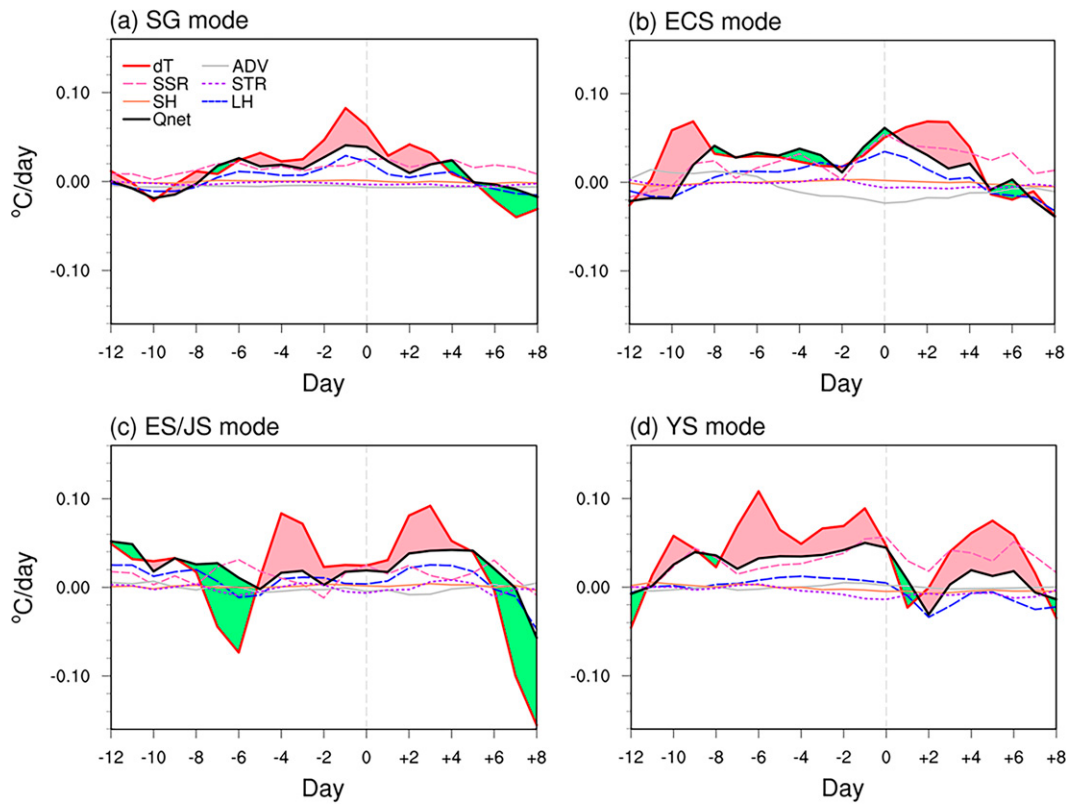


FIG. 8. Time series of anomalous mixed-layer temperature and horizontal advection from GLORYS12 and heat fluxes from ERA5 (lines; $^{\circ}\text{C day}^{-1}$) averaged over each black box in Fig. 4 from days -12 to $+8$ during the period 1993–2020 for the (a) SG, (b) ECS, (c) ES/JS, and (d) YS modes. dT and ADV represents the mixed-layer temperature tendency and horizontal advection, respectively. The abbreviations SSR, STR, SH, and LH stand for surface shortwave radiation, surface thermal radiation, sensible heat flux, and latent heat flux, respectively. Qnet indicates the net surface heat fluxes. The pink (green) shading indicates positive (negative) vertical term including vertical advection, mixing, entrainment/detrainment. For each MHW, the onset date was defined as day 0, and dates before and after are given as negative and positive days, respectively.

heat fluxes before and after the onset date to examine the possible mechanisms that cause and maintain MHWs (Fig. 8).

In the SG mode, the mixed-layer temperature tendencies were approximately analogous to the net sums of the surface heat flux (Fig. 8a). Both shortwave radiation and wind-induced Ekman downwelling mainly contribute to warm water temperatures before the occurrence of MHWs, indicating that the WNPSH has had a significant impact on the development of MHWs. This mode lasted for approximately 5.17 days (Table 1), and the decline of the MHWs was attributed to Ekman upwelling and negative latent heat flux as a result of enhanced surface wind speeds (figure not shown). In the ECS mode, shortwave radiation was negative, and longwave radiation was positive until 10 days prior to the onset of MHWs, which implies that clouds covered these areas during this period (Fig. 8b) (Kiehl and Trenberth 1997). This interpretation is supported by the relationship between the ECS mode and the retreat date of the rainy season. Figure 9 shows the time–latitude evolution of precipitation and atmospheric circulations before and after the onset of the ECS mode. A few days before the onset, the increase in precipitation

was apparent along 30°N . When the EASM intensity was strong, the freshwater from the Yangtze River (also called the Changjiang River) or rainfall itself in the East China Sea would lead to a shallow surface layer of freshwater in a few days and maintain a vertical salinity gradient (i.e., barrier layer formation) (Fig. 10b), resulting in suppressed vertical mixing and the extreme MHWs (Fig. 8b) (Belkin 2009; Park et al. 2011). Moreover, as the westerly jet moved north, the rainband gradually shifted northward, and it was displaced by the anomalous anticyclonic circulation (Figs. 5b, 9) (Oh and Ha 2020). The enhanced anticyclone enhanced downward shortwave radiation, resulting in surface warming in the East China Sea (Fig. 8b). Both the oceanic (suppressed vertical mixing) and atmospheric effects (enhanced shortwave radiation) are responsible for the MHWs. Regarding the retreat of MHWs in the East China Sea, the negative (upward) latent heat flux due to large sea–air humidity differences (figure not shown) can remarkably reduce the MHWs (Fig. 8b).

Due to strong thermal stratification, not only atmosphere–ocean heat exchanges (positive shortwave radiation and latent

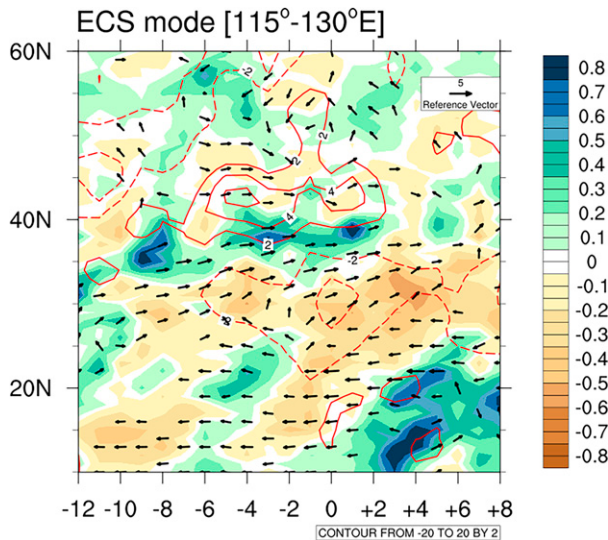


FIG. 9. Time–latitude plot of anomalous precipitation (mm day^{-1} ; shading), zonal wind at 200 hPa (m s^{-1} ; red line), and wind at 850 hPa (m s^{-1} ; vectors) averaged over $115^{\circ}\text{--}130^{\circ}\text{E}$ from days -12 to $+8$ for the ECS mode. The onset date was defined as day 0, and dates before and after are shown as negative and positive days, respectively.

heat flux), but also less vertical mixing would enhance surface warming in the ES/JS mode during the growing period of MHWs (Figs. 8c and 10c). The stratification eventually reduced entrainment cooling in the same region (Wang et al. 2022), thereby maintaining warm water conditions. The warming tendencies weakened approximately five days after onset, which was attributed to negative vertical terms, showing a stronger Ekman upwelling. Simultaneously, the ocean dynamics related to surface wind stress curl can result in convergence/divergence in the surface water, thereby changing water temperature (Liu et al. 2022). In the ES/JS mode, the positive wind stress curl might have contributed to the weakening of the MHWs by inducing wind-driven-Ekman upwelling (figure not shown). It enhances entrainment cooling and reduces MHW-related SST warming. In the YS mode, a strong warming tendency persisted until seven days after the onset of MHWs and remained longer than in the SG and ES/JS modes (Fig. 8d). The long-lasting warming was mainly attributed to the shortwave radiation due to anticyclonic circulation (Fig. 5d) and ocean dynamics such as stratification by low-salinity and extreme warm water of the mixed layer (Fig. 10d). There were few key differences between the ECS and YS modes. Both modes had longer-lasting MHWs than the other two modes, and they were also associated with the strong stratification caused by the low-salinity water. However, ECS mode was strongly affected by low-salinity water from the Yangtze River after a strong EASM, namely, heavy rainfall in China and its surroundings. We observed a delayed connection between the inflow of low-salinity and warm temperature in the ECS mode (Fig. 10b). After the rainband moves to the north, the freshwater from the Yangtze River due to strong monsoon rainfall would maintain strong density stratification by acting as a barrier, which suppresses vertical mixing that can

contribute to warm water, together with the atmospheric effect. However, low-salinity water in the YS mode coincides with the warm water, indicating that the low-salinity water and the hot water could have resulted from the southerly wind (Lee et al. 2015) by the anticyclonic circulation (Figs. 8d and 10d). The MHWs in the YS mode could be maintained due to the stratification by locally driven low-salinity water, but whether the low-salinity of the Yangtze River generates them remains inconclusive.

c. Impact of remote forcings on East Asian MHWs

The SG mode could be explained by a warming-related mode, and the ECS mode tended to be linked to the EASM retreat. Thus, it is important to identify what causes MHWs in the ES/JS and YS modes. We inferred that anticyclonic circulation had already been established a few days before the onset via positive shortwave radiation (Figs. 8c,d). Therefore, identifying the distinguishing tropical–subtropical forcing(s) that can generate the atmospheric responses for the two modes is crucial. Figure 11 displays the composite maps of anomalous upper-level vorticity (vorticity forcing) and anomalous precipitation (thermal forcing) for the two modes. The negative vorticity at the upper level over the Mediterranean and positive precipitation anomalies over India and the western Pacific were distributed in the ES/JS mode. Moreover, we found that the heavy rainfall over India, the South China Sea, and WNP could be thermal forcings for the YS modes.

Based on these remote forcings, a linear baroclinic model (LBM)-based experiment was performed with the mean summer climatological data from 1982 to 2020 (Watanabe and Kimoto 2000). The model had a horizontal resolution of T42 and 20 sigma levels (i.e., T42L20) and it was integrated for up to 30 days to approach a steady atmospheric response to the prescribed forcings. We achieved a mean of nine days' integration for the near steady state from the simulation. Distinctive positions of the forcings between the ES/JS and YS modes were based on the distribution of the vorticity forcing and atmospheric diabatic heating over the tropics and subtropics (Figs. 11a,b). The prescribed steady forcing can generate atmospheric Rossby wave propagation. Thus, we prescribed idealized forcing with respect to the composite differences in negative vorticity forcing (40°N , 30°E) and thermal forcing (i.e., precipitation) (20°N , 70°E) for the ES/JS mode and thermal forcings (20°N , 70°E ; 20°N , 115°E ; and 15°N , 130°E) for the YS mode. Son et al. (2021) described that negative vorticity forcing, linked to westward propagating tropical waves by the thermal forcing over India, could contribute to the generation of teleconnection in the Northern Hemisphere heading to East Asia during boreal summer. G.-U. Kim et al. (2019) also showed that the Indian monsoon heating induced the descending motion over the Mediterranean Sea via the Gill-type Rossby wave response. Note that the thermal forcing over the WNP in the ES/JS played a minor role in inducing the atmospheric circulation change. For the ES/JS mode, the thermal forcing over India (20°N , 70°E) might lead the westward-propagating tropical Rossby waves to the northwest, and the resultant vorticity forcing over the Mediterranean excites eastward-propagating

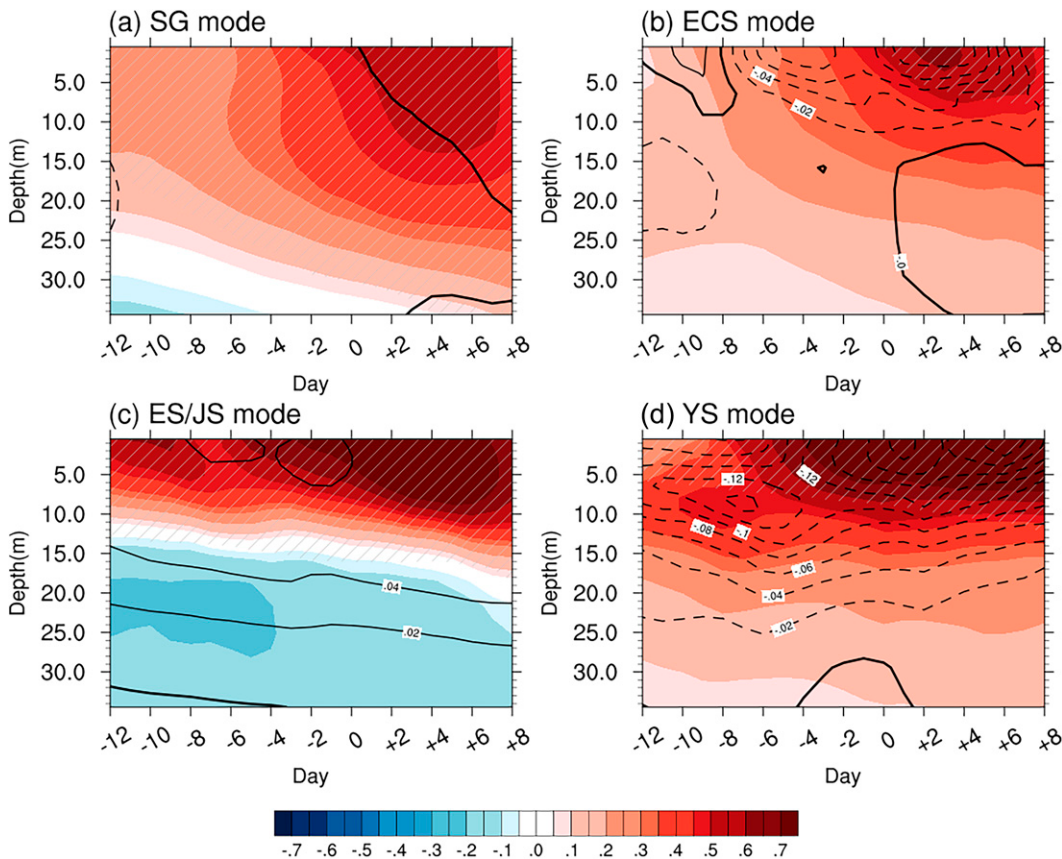


FIG. 10. Time–depth plots of anomalous water temperature ($^{\circ}$ C; shading) and salinity (psu; contours) from GLORYS12 averaged over each black box in Fig. 4 from days -12 to $+8$ for the (a) Subtropical Gyre (SG), (b) East China Sea (ECS), (c) East Sea/Japan Sea (ES/JS), and (d) Yellow Sea (YS) modes. For each marine heatwave (MHW), the onset date was defined as day 0, and dates before and after are shown as negative and positive days, respectively. The gray hatched lines indicate the significant area for the water temperature at $p < 0.05$.

barotropic structures at the midlatitude, resulting in anticyclonic circulation across East Asia (Fig. 11a). We observed that the wave activity flux started from the Mediterranean propagates to East Asia. In the YS mode experiment, the anticyclonic circulation over inland China was induced by thermal forcing over the South China Sea and the WNP propagates to the north via the Rossby wave propagation. The wave propagation strengthens anticyclonic circulation to the east and midlatitude cyclone over northern Japan (east–west zonal dipole pattern) (Fig. 11b). Therefore, the ES/JS and YS modes were classified according to the locations of their subtropical forcings, and could be important precursors to MHWs in these two modes.

4. Summary

Here, we classified four modes of the MHWs across East Asia using SOM analysis and quantified the contributions of air-sea interactions to MHWs for each mode. To determine this, we conducted an EOF analysis with the boreal summer SST anomalies when the MHWs occurred (854 days) to obtain their PC time series prior to SOM analysis. The first three PCs of the SSTs for the 854 MHW days were used to

construct 2×2 maps containing information about the clustered dates. We mapped the spatial distributions of the atmospheric and oceanic variables by composing the classified dates for each mode. Our results show that SOM analysis can be used to effectively distinguish the regional characteristics of MHWs on a subseasonal time scale.

The spatial distribution of SSTs in the SG mode was similar to the increasing trend pattern for the duration of MHWs across East Asia. We also observed that the mode showed a clear trend in the annual number of clustered days from 1982 to 2020. Considering both the spatial and temporal information, we expect this mode to increase further. In the case of the ECS mode, the positive longwave radiation and negative shortwave radiation values were conspicuous before the onset of the MHWs, which implies that clouds covered these areas. This mode is related to retreat of the EASM. The EASM has retreated northward, and it was displaced by the anomalous anticyclonic circulation enhancing downward shortwave radiation. Simultaneously, there was a significant ocean effect on the MHWs in the ECS mode. After the rainband retreated to the north, the freshwater from the Yangtze River due to the strong monsoon rainfall maintained strong density stratification

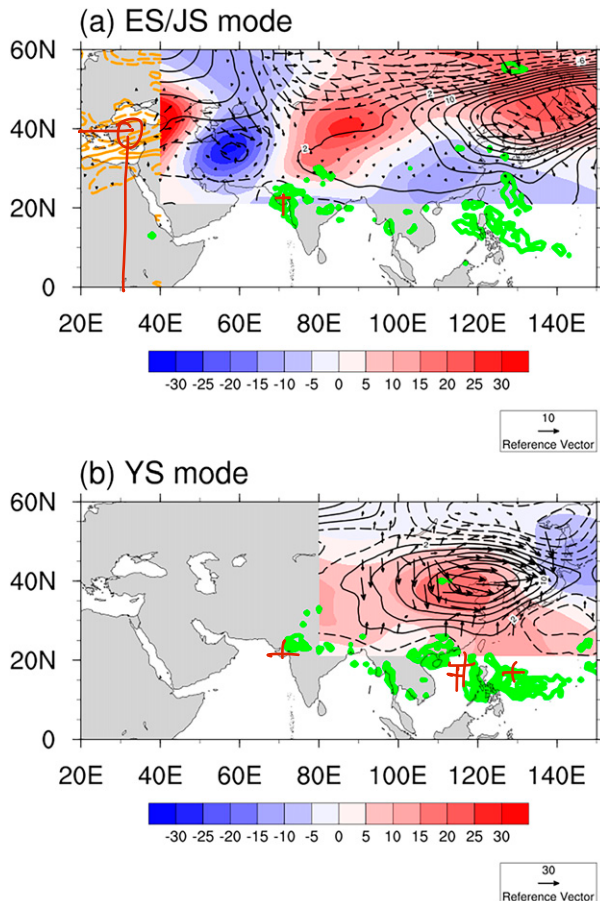


FIG. 11. Composite map of anomalous geopotential height at 500 hPa (m; contours), vorticity at 200 hPa (orange lines), and precipitation (green lines) for the (a) East Sea/Japan Sea (ES/JS) and (b) Yellow Sea (YS) modes, and simulated 500-hPa geopotential height anomalies (m; shading) in response to tropical–subtropical forcings. The green lines show anomalous precipitation; only values above 0.1 mm day^{-1} are plotted. The orange lines are anomalous vorticity at 200 hPa; only negative values are plotted in (a). The black vectors indicate wave activity flux at 200 hPa. The idealized forcing for the linear baroclinic model was adopted from the negative vorticity centered at 40°N , 30°E and positive diabatic heating centered at 20°N , 70°E (positive diabatic heating centered at 20°N , 70°E ; 20°N , 115°E ; and 15°N , 130°E) for the ES/JS (YS) mode. The correlations between the observed and the idealized patterns over the area shown in the figures for the ES/JS and YS were $r = 0.55$ and $r = 0.60$, respectively, both of which are significant at a 95% confidence level.

by acting as a barrier, which suppresses vertical mixing and gives rise to positive local feedback that can contribute to warm water. It can be captured using observational station data (e.g., the Ieodo and Socheongcho stations). Thus, the development of the MHWs in the East China Sea can be explained by both atmospheric and oceanic perspectives. The MHWs in the ES/JS mode were also dominated by heat fluxes and oceanic dynamics, namely weaker entrainment cooling caused by the enhanced Ekman downwelling. Furthermore, the wind-induced Ekman upwelling played an important role

in the decline of the MHWs in the ES/JS mode. In the YS mode, enhanced shortwave radiation played essential roles in SST warming for the onset of MHWs due to anticyclonic circulation. The weaker entrainment cooling by reduced vertical mixing largely also contributed to the growth of MHWs.

The ES/JS and YS modes were connected to the midlatitude and subtropical wave trains from the vorticity and thermal forcings. Thus, an LBM experiment was performed to understand the causes of these modes originating from tropical–subtropical forcings. The distinct forcings were distributed in the two modes. The negative upper-level vorticity forcing over the Mediterranean, which might be caused by thermal forcing over India, resulted in atmospheric responses with enhanced anticyclonic activity across East Asia through Rossby wave propagation for the ES/JS mode. In the YS mode, thermal forcing over India, the South China Sea, and the WNP induced a dipole pattern across East Asia, causing the anticyclone to the west and the cyclone to the east, which were interpreted as Rossby wave responses. The characteristics of the four MHW modes were remarkably different, and it is expected that their distinctive precursory signals can improve the prediction of EAMS.

The SG mode exhibited a significant increasing trend on the interannual time scale (Fig. 4e), which may be linked to global warming. Moreover, the SG mode also displayed the strongest Atlantic warming among the modes, resembling the positive Atlantic multidecadal oscillation (AMO) pattern (Wu et al. 2020). Thus, we cannot be certain whether or not the SG mode was affected by anthropogenic forcing because the AMO has been positive since the 1990s. Further studies are needed to examine the relative roles of internal variation and anthropogenic forcing using various future scenarios in phase 6 of the Coupled Model Intercomparison Project. Furthermore, this study suggested that subtropical convection could act as a precursor for East Asian MHWs. The boreal summer intraseasonal oscillation (BSISO) is likely linked to the East Asian MHWs as the subtropical forcing. Hsu et al. (2017) discovered that BSISO-related circulation patterns leads to favorable conditions for atmospheric heatwaves across the WNP and East Asia. The energized ISO could strengthen the WNPSH (Wang et al. 2019), which modulates the MHWs across East Asia. The four modes, which occur over time, are likely to be a local manifestation of a meridional displacement of the WNPSH (Choi and Kim 2019; Chu et al. 2012; Oh and Ha 2015). Therefore, further study is necessary to understand the characteristics of MHWs in East Asia according to BSISO phases.

Acknowledgments. This work was supported by the National Research Foundation of Korea (NRF) grant funded by the Korea government (MSIT) (No. 2021R1C1C2005002). This research was supported by Korea Institute of Marine Science & Technology Promotion (KIMST) funded by the Ministry of Oceans and Fisheries (20210607, Establishment of the Ocean Research Station in the Jurisdiction Zone and Convergence Research). C. J. Jang was supported by the NRF grant funded by the MSIT (Grant NRF-2020R1F1A1072447).

Data availability statement. Daily OISST data were downloaded from <https://psl.noaa.gov/data/gridded/data.noaa.oisst.v2.highres.html> and hourly ERA5 data on pressure levels (for a single level) are available at <https://cds.climate.copernicus.eu/cdsapp#!/dataset/reanalysis-era5-pressure-levels?tab=form> (<https://cds.climate.copernicus.eu/cdsapp#!/dataset/reanalysis-era5-single-levels-monthly-means?tab=form>). Daily GLORYS12 data were obtained from https://data.marine.copernicus.eu/product/GLOBAL_MULTIYEAR_PHY_001_030/services. Data from in situ measurements, including the Ieodo and Socheongcho stations, are accessible at <https://kors.kiost.ac.kr/en/>.

REFERENCES

- Amaya, D. J., A. J. Miller, S.-P. Xie, and Y. Kosaka, 2020: Physical drivers of the summer 2019 North Pacific marine heatwave. *Nat. Commun.*, **11**, 1903, <https://doi.org/10.1038/s41467-020-15820-w>.
- Belkin, I. M., 2009: Rapid warming of large marine ecosystems. *Prog. Oceanogr.*, **81**, 207–213, <https://doi.org/10.1016/j.pocean.2009.04.011>.
- Bond, N. A., M. F. Cronin, H. Freeland, and N. Mantua, 2015: Causes and impacts of the 2014 warm anomaly in the NE Pacific. *Geophys. Res. Lett.*, **42**, 3414–3420, <https://doi.org/10.1002/2015GL063306>.
- Choi, W., and K.-Y. Kim, 2019: Summertime variability of the western North Pacific subtropical high and its synoptic influences on the East Asian weather. *Sci. Rep.*, **9**, 7865, <https://doi.org/10.1038/s41598-019-44414-w>.
- Chu, J.-E., S. N. Hameed, and K.-J. Ha, 2012: Nonlinear, intraseasonal phases of the East Asian summer monsoon: Extraction and analysis using self-organizing maps. *J. Climate*, **25**, 6975–6988, <https://doi.org/10.1175/JCLI-D-11-00512.1>.
- Feng, M., M. J. McPhaden, S.-P. Xie, and J. Hafner, 2013: La Niña forces unprecedented Leeuwin Current warming in 2011. *Sci. Rep.*, **3**, 1277, <https://doi.org/10.1038/srep01277>.
- Frölicher, T. L., and C. Laufkötter, 2018: Emerging risks from marine heat waves. *Nat. Commun.*, **9**, 650, <https://doi.org/10.1038/s41467-018-03163-6>.
- , E. M. Fischer, and N. Gruber, 2018: Marine heatwaves under global warming. *Nature*, **560**, 360–364, <https://doi.org/10.1038/s41586-018-0383-9>.
- Gao, G., M. Marin, M. Feng, B. Yin, D. Yang, X. Feng, Y. Ding, and D. Song, 2020: Drivers of marine heatwaves in the East China Sea and the South Yellow Sea in three consecutive summers during 2016–2018. *J. Geophys. Res. Oceans*, **125**, e2020JC016518, <https://doi.org/10.1029/2020JC016518>.
- , X. Zhao, M. Jiang, and L. Gao, 2021: Impacts of marine heatwaves on algal structure and carbon sequestration in conjunction with ocean warming and acidification. *Front. Mar. Sci.*, **8**, 758651, <https://doi.org/10.3389/fmars.2021.758651>.
- Ha, K.-J., and Coauthors, 2019: Observations utilizing Korea Ocean Research Stations and their applications for process studies. *Bull. Amer. Meteor. Soc.*, **100**, 2061–2075, <https://doi.org/10.1175/BAMS-D-18-0305.1>.
- Heo, K.-Y., K.-J. Ha, L. Mahrt, and J.-S. Shim, 2010: Comparison of advection and steam fogs: From direct observation over the sea. *Atmos. Res.*, **98**, 426–437, <https://doi.org/10.1016/j.atmosres.2010.08.004>.
- Hersbach, H., and Coauthors, 2020: The ERA5 global reanalysis. *Quart. J. Roy. Meteor. Soc.*, **146**, 1999–2049, <https://doi.org/10.1002/qj.3803>.
- Hobday, A. J., and Coauthors, 2016: A hierarchical approach to defining marine heatwaves. *Prog. Oceanogr.*, **141**, 227–238, <https://doi.org/10.1016/j.pocean.2015.12.014>.
- Holbrook, N. J., and Coauthors, 2019: A global assessment of marine heatwaves and their drivers. *Nat. Commun.*, **10**, 2624, <https://doi.org/10.1038/s41467-019-10206-z>.
- Hsu, P.-C., J.-Y. Lee, K.-J. Ha, and C.-H. Tsou, 2017: Influences of boreal summer intraseasonal oscillation on heat waves in monsoon Asia. *J. Climate*, **30**, 7191–7211, <https://doi.org/10.1175/JCLI-D-16-0505.1>.
- Huang, B., C. Liu, V. Banzon, E. Freeman, G. Graham, B. Hankins, T. Smith, and H.-M. Zhang, 2021: Improvements of the Daily Optimum Interpolation Sea Surface Temperature (DOISST) version 2.1. *J. Climate*, **34**, 2923–2939, <https://doi.org/10.1175/JCLI-D-20-0166.1>.
- Hughes, T. P., and Coauthors, 2018: Global warming transforms coral reef assemblages. *Nature*, **556**, 492–496, <https://doi.org/10.1038/s41586-018-0041-2>.
- Johnson, N. C., 2013: How many ENSO flavors can we distinguish? *J. Climate*, **26**, 4816–4827, <https://doi.org/10.1175/JCLI-D-12-0049.1>.
- Kiehl, J. T., and K. E. Trenberth, 1997: Earth's annual global mean energy budget. *Bull. Amer. Meteor. Soc.*, **78**, 197–208, [https://doi.org/10.1175/1520-0477\(1997\)078<0197:EAGMEB>2.0.CO;2](https://doi.org/10.1175/1520-0477(1997)078<0197:EAGMEB>2.0.CO;2).
- Kim, G.-U., K.-H. Seo, and D. Chen, 2019: Climate change over the Mediterranean and current destruction of marine ecosystem. *Sci. Rep.*, **9**, 18813, <https://doi.org/10.1038/s41598-019-55303-7>.
- , and Coauthors, 2022: Record-breaking slow temperature evolution of spring water during 2020 and its impacts on spring bloom in the Yellow Sea. *Front. Mar. Sci.*, **9**, 824361, <https://doi.org/10.3389/fmars.2022.824361>.
- Kim, H.-K., and K.-H. Seo, 2016: Cluster analysis of tropical cyclone tracks over the western North Pacific using a self-organizing map. *J. Climate*, **29**, 3731–3751, <https://doi.org/10.1175/JCLI-D-15-0380.1>.
- Kim, Y. S., and Coauthors, 2019: A Yellow Sea monitoring platform and its scientific applications. *Front. Mar. Sci.*, **6**, 601, <https://doi.org/10.3389/fmars.2019.00601>.
- Kohonen, T., 1990: The self-organizing map. *Proc. IEEE*, **78**, 1464–1480, <https://doi.org/10.1109/5.58325>.
- Kuroda, H., and T. Setou, 2021: Extensive marine heatwaves at the sea surface in the northwestern Pacific Ocean in summer 2021. *Remote Sens.*, **13**, 3989, <https://doi.org/10.3390/rs13193989>.
- Kwon, Y.-Y., J.-Y. Jeong, J.-Y. Choi, J.-S. Shim, S.-K. Hyun, and J.-I. Kwon, 2012: Simulation of vertical water temperature structure variation in the Yellow Sea typhoon MEARI. *J. Coastal Res.*, **85**, 1016–1020, <https://doi.org/10.2112/SI85-2041>.
- Lee, D.-K., J.-I. Kwon, and S. Son, 2015: Horizontal distribution of Changjiang diluted water in summer inferred from total suspended sediment in the Yellow Sea and East China Sea. *Acta Oceanol. Sin.*, **34**, 44–50, <https://doi.org/10.1007/s13131-015-0776-7>.
- Lee, S., M.-S. Park, M. Kwon, Y. H. Kim, and Y.-G. Park, 2020: Two major modes of East Asian marine heatwaves. *Environ. Res. Lett.*, **15**, 074008, <https://doi.org/10.1088/1748-9326/ab8527>.

- Lellouche, J.-M., and Coauthors, 2021: The Copernicus global 1/12° oceanic and sea ice GLORYS12 reanalysis. *Front. Earth Sci.*, **9**, 698876, <https://doi.org/10.3389/feart.2021.698876>.
- Li, Y., G. Ren, Q. Wang, and Q. You, 2019: More extreme marine heatwaves in the China Seas during the global warming hiatus. *Environ. Res. Lett.*, **14**, 104010, <https://doi.org/10.1088/1748-9326/ab28bc>.
- , —, Q. You, Q. Wang, Q. Niu, and L. Mu, 2022: The 2016 record-breaking marine heatwave in the Yellow Sea and associated atmospheric circulation anomalies. *Atmos. Res.*, **268**, 106011, <https://doi.org/10.1016/j.atmosres.2021.106011>.
- Liu, K., K. Xu, C. Zhu, and B. Liu, 2022: Diversity of marine heatwaves in the South China Sea regulated by ENSO phase. *J. Climate*, **35**, 877–893, <https://doi.org/10.1175/JCLI-D-21-0309.1>.
- Moisan, J. R., and P. P. Niiler, 1998: The seasonal heat budget of the North Pacific: Net heat flux and heat storage rates (1950–1990). *J. Phys. Oceanogr.*, **28**, 401–421, [https://doi.org/10.1175/1520-0485\(1998\)028<0401:TSHBOT>2.0.CO;2](https://doi.org/10.1175/1520-0485(1998)028<0401:TSHBOT>2.0.CO;2).
- Moon, I.-J., and S. J. Kwon, 2012: Impact of upper-ocean thermal structure on the intensity of Korean Peninsular landfall typhoons. *Prog. Oceanogr.*, **105**, 61–66, <https://doi.org/10.1016/j.pocean.2012.04.008>.
- Moon, J.-H., T. Kim, Y. B. Son, J.-S. Hong, J.-H. Lee, P.-H. Chang, and S.-K. Kim, 2019: Contribution of low-salinity water to sea surface warming of the East China Sea in the summer of 2016. *Prog. Oceanogr.*, **175**, 68–80, <https://doi.org/10.1016/j.pocean.2019.03.012>.
- Oh, H., and K.-J. Ha, 2015: Thermodynamic characteristics and responses to ENSO of dominant intraseasonal modes in the East Asian summer monsoon. *Climate Dyn.*, **44**, 1751–1766, <https://doi.org/10.1007/s00382-014-2268-4>.
- , —, 2020: Role of the surface boundary conditions in boreal spring on the interannual variability of the multistage evolution of the East Asian summer monsoon. *J. Climate*, **33**, 1845–1861, <https://doi.org/10.1175/JCLI-D-19-0249.1>.
- , —, and J.-S. Shim, 2014: Analysis for onset of Changma using Ieodo ocean research station data. *Atmosphere*, **24**, 189–196, <https://doi.org/10.14191/Atmos.2014.24.2.189>.
- Oh, H.-R., and Coauthors, 2020: Impact of Chinese air pollutants on a record-breaking PMs episode in the Republic of Korea for 11–15 January 2019. *Atmos. Environ.*, **223**, 117262, <https://doi.org/10.1016/j.atmosenv.2020.117262>.
- Oliver, E. C. J. 2019: Mean warming not variability drives marine heatwave trends. *Climate Dyn.*, **53**, 1653–1659, <https://doi.org/10.1007/s00382-019-04707-2>.
- , J. A. Benthuysen, N. L. Bindoff, A. J. Hobday, N. J. Holbrook, C. N. Mundy, and S. E. Perkins-Kirkpatrick, 2017: The unprecedented 2015/16 Tasman Sea marine heatwave. *Nat. Commun.*, **8**, 16101, <https://doi.org/10.1038/ncomms16101>.
- , V. Lago, A. J. Hobday, N. J. Holbrook, S. D. Ling, and C. N. Mundy, 2018: Marine heatwaves off eastern Tasmania: Trends, interannual variability, and predictability. *Prog. Oceanogr.*, **161**, 116–130, <https://doi.org/10.1016/j.pocean.2018.02.007>.
- Park, T., C. J. Jang, J. H. Jungclaus, H. Haak, W. Park, and I. S. Oh, 2011: Effects of the Changjiang river discharge on sea surface warming in the Yellow and East China Seas in summer. *Cont. Shelf Res.*, **31**, 15–22, <https://doi.org/10.1016/j.csr.2010.10.012>.
- Plecha, S. M., and P. M. M. Soares, 2020: Global marine heatwave events using the new CMIP6 multi-model ensemble: From shortcomings in present climate to future projections. *Environ. Res. Lett.*, **15**, 124058, <https://doi.org/10.1088/1748-9326/abc847>.
- Qiu, Z., F. Qiao, C. J. Jang, L. Zhang, and Z. Song, 2021: Evaluation and projection of global marine heatwaves based on CMIP6 models. *Deep-Sea Res. II*, **194**, 104998, <https://doi.org/10.1016/j.dsr2.2021.104998>.
- Ren, L., T. Zhou, and W. Zhang, 2020: Attribution of the record-breaking heat event over Northeast Asia in summer 2018: The role of circulation. *Environ. Res. Lett.*, **15**, 054018, <https://doi.org/10.1088/1748-9326/ab8032>.
- Reynolds, R. W., T. M. Smith, C. Liu, D. B. Chelton, K. S. Casey, and M. G. Schlax, 2007: Daily high-resolution-blended analyses for sea surface temperature. *J. Climate*, **20**, 5473–5496, <https://doi.org/10.1175/2007JCLI1824.1>.
- Schlegel, R. W., E. C. J. Oliver, A. J. Smit, S. Perkins-Kirkpatrick, and A. Kruger, 2017: Predominant atmospheric and oceanic patterns during coastal marine heatwaves. *Front. Mar. Sci.*, **4**, 323, <https://doi.org/10.3389/fmars.2017.00323>.
- Son, J.-H., K.-H. Seo, S.-W. Son, and D.-H. Cha, 2021: How does Indian monsoon regulate the Northern Hemisphere stationary wave pattern? *Front. Earth Sci.*, **8**, 599745, <https://doi.org/10.3389/feart.2020.599745>.
- Wang, D., T. Xu, G. Fang, S. Jiang, G. Wang, Z. Wie, and Y. Wang, 2022: Characteristics of marine heatwaves in the Japan/East Sea. *Remote Sens.*, **14**, 936, <https://doi.org/10.3390/rs14040936>.
- Wang, S. S.-Y., H. Kim, D. Coumou, J.-H. Yoon, L. Zhao, and R. R. Gillies, 2019: Consecutive extreme flooding and heat wave in Japan: Are they becoming a norm? *Atmos. Sci. Lett.*, **20**, e933, <https://doi.org/10.1002/asl.933>.
- Watanabe, M., and M. Kimoto, 2000: Atmosphere–ocean thermal coupling in the North Atlantic: A positive feedback. *Quart. J. Roy. Meteor. Soc.*, **126**, 3343–3369, <https://doi.org/10.1002/qj.49712657017>.
- Wu, B., X. Lin, and L. Yu, 2020: North Pacific subtropical mode water is controlled by the Atlantic multidecadal variability. *Nat. Climate Change*, **10**, 238–243, <https://doi.org/10.1038/s41558-020-0692-5>.
- Yan, Y., F. Chai, H. Xue, and G. Wang, 2020: Record-breaking sea surface temperatures in the Yellow and East China Seas. *J. Geophys. Res. Oceans*, **125**, e2019JC015883, <https://doi.org/10.1029/2019JC015883>.
- Yao, Y., and C. Wang, 2021: Variations in summer marine heatwaves in the South China Sea. *J. Geophys. Res. Oceans*, **126**, e2021JC017792, <https://doi.org/10.1029/2021JC017792>.
- , J. Wang, J. Yin, and X. Zou, 2020: Marine heatwaves in China's marginal seas and adjacent offshore waters: Past, present, and future. *J. Geophys. Res. Oceans*, **125**, e2019JC015801, <https://doi.org/10.1029/2019JC015801>.
- Yeo, S.-R., S.-W. Yeh, and W.-S. Lee, 2019: Two types of heat wave in Korea associated with atmospheric circulation pattern. *J. Geophys. Res. Atmos.*, **124**, 7498–7511, <https://doi.org/10.1029/2018JD030170>.
- Yun, J., and K.-J. Ha, 2022: Physical processes in sea fog formation and characteristics of turbulent air-sea fluxes at Sacheongcho Ocean research station in the Yellow Sea. *Front. Mar. Sci.*, **9**, 825973, <https://doi.org/10.3389/fmars.2022.825973>.